Pose Measurement and Contact Training of a Fabric-reinforced Inflatable Soft Robot

Phuc D.H. Bui[1] and Joshua A. Schultz[1]

***Abstract*— This paper proposes a new method to measure the pose and localize the contacts with the surrounding environment for an inflatable soft robot by using optical sensors (photocells), inertial measurement units (IMUs), and a pressure sensor. These affordable sensors reside entirely aboard the robot and will be effective in environments where external sensors, such as motion capture, are not feasible to use. The entire bore of the robot is used as a waveguide to transfer the light. When the robot is working, the photocell signals vary with the current shape of the robot and the IMUs measure the orientation of its tip. Analytical functions are developed to relate the photocell signals and the robot pose. Since the soft robot is deformable, the occurrence of contact at any location on its body will modify the sensor signals. This simple measurement approach generates enough information to allow contact events to be detected and classified with high precision using a machine learning algorithm.**

I. INTRODUCTION

Soft robots are designed with soft bodies and completion of tasks may involve contacts with any part of their bodies, not just their tips. Because they are made of soft materials, soft robots will be compliant in response to their environment, interact more safely with humans, and survive after collisions or falls. Since the body of a soft robot is a continuum, reconstructing its motions using sensory feedback is challenging [1] [2], especially when the robot makes contact with the environment.

There have been many soft sensing approaches proposed to measure the pose of soft robots. The most popular ones are based on resistive strain sensors [3], [4], [5], capacitive strain sensors [6], [7], [8], and optical waveguide sensors [9], [10], [11], [12], [13]. Among these sensing strategies, optical waveguide sensors tend to be more reliable because they can avoid soft-rigid connections between the sensing parts [2]. It can be found that nearly all existing optical sensing methods used optical fibers or created a standalone stretchable waveguide so that the light can propagate internally. Those sensors can track the bending or expansion of the soft robots. However, it's extremely technologically complex for them to perform tactile sensing to detect contacts at various locations on the body of the soft robots. Furthermore, embedding those sensors would also change the stiffness of the surrounding elastomer matrix where it is located.

This work is supported by the NSF grant No. 1935312 EFRI C3 SoRo: Between a Soft Robot and a Hard Place: Estimation and Control Algorithms that Exploit Soft Robots' Unique Abilities

[1]The authors are with Department of Mechanical Engineering, The University of Tulsa, 800 S. Tucker Drive, Tulsa, OK 74104, USA. phuc-bui@utulsa.edu, joshua-schultz@utulsa.edu

In efforts to create tactile sensing similar to that of human skin, researchers have created several examples of electronic "skin" for robotics applications, such as the smart braid [14], E-skin [15], electronic skin [16], and artificial skin [17]. However, the techniques are still in their infancy and applications are still very limited. The challenges include sensor integration, the embedding of high-resolution but large-area sensor arrays, and sensor fusion with increasing volumes of data [16].

In this study, instead of using tactile skin, we propose a sensing approach that enables the soft robot to localize contact events using photocells, IMUs, and a pressure sensor. These sensors can also track the current pose of the robot in free space. They are much easier to implement than tactile sensors. We installed these sensors in our soft robot "Squishy" [18] [19] which is an inflatable elastomeric chamber made of Smooth-On Dragon Skin 30 silicone with a thin band of fabric embedded longitudinally to reinforce one side (see Fig. 1). More information about its characteristics, such as the workspace volume and inflation-displacement behavior can be found in [20]. The novel idea in this work is that we used the entire bore of the robot chamber as a waveguide to transmit the light. When inflated pneumatically, the unreinforced side can undergo large strains while the fabric side maintains a constant length, causing the chamber to bend and turn. Due to the original shape of the chamber and the calculated position of the fabric, the robot can perform a motion in $\mathbb{R}^3$ space with only a single chamber.

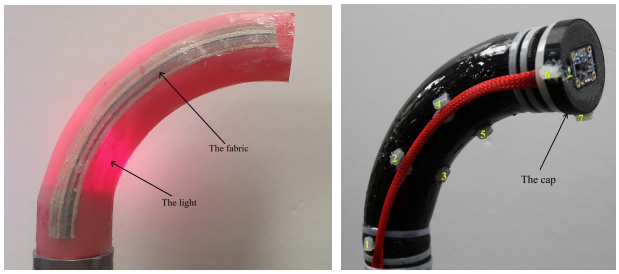

(a) (b)

Fig. 1. Soft robot Squishy: (a) The robot before painting the outer surface shows the embedded fabric, the light source at the base and red color inside; (b) Completed robot with the black paint outside and the cap. The numbers on its body show the positions of ground-truth sensors.

The light source is installed at the base of the robot chamber and four photocells are installed at the tip. When the soft robot's shape is changing or making contact with the environment, the light incident on each photocell varies, depending on the illumination reflected by the chamber

2023 IEEE/SICE International Symposium on System Integration (SII) | 979-8-3503-9868-7/23/$31.00 ©2023 IEEE | DOI: 10.1109/SII55687.2023.10039331

wall. Thus, the voltages from the photocells will have a relationship with the states of the robot. The relationship will be calculated through developed analytical equations.

In addition to the photocells, a pair of IMUs is installed at the tip of the robot. They provide information about the tip's orientation with roll, pitch, and yaw angle. These IMUs also generate richer information to support the classification process used in defining contact events. The Random Forest algorithm will be applied to classify contact events using contact data from the sensors. Besides the ability to perform both shape measurement and contact localization, this sensing approach also has other advantages: the sensors are affordable and easy to install, they do not affect the elasticity of the host robot, and they are embedded entirely within the robot, allowing it to be used in the field with no need to instrument the environment. This study contributes a sensing approach that can help the soft robot sense not only its current pose but also contacts on its body, which is unable to be achieved by the other sensing approaches.

The rest of this paper is structured as follows. In Section II, we describe the configuration of the sensors and the acquisition of sensor signals. Section III is about how to reconstruct the configuration of the soft robot from the sensor measurements. Section IV describes the strategy for characterizing contact events and training the robot to recognize the contact location and direction. In section V we experimentally evaluate the proposed approach and compare with simulation results. Section VI concludes the work.

II. Sensor Configuration and Signal Acquisition

A. Optical Sensing

The body of the robot is a fabric-reinforced silicone chamber. The space inside the chamber contains nothing but air. Therefore, we can use the entire body of the robot as the waveguide for the light. We placed a white light-emitting diode (LED) (Adafruit 754) at the robot's base to serve as the light source (see Fig. 1a). To measure the light, we installed four mini photocells (Sparkfun GL5528) on the inner-side surface of the cap as shown in Fig. 2, where photocell number 4 is aligned with the fabric. This photocell has a quick response, small size, high sensitivity, and reliable performance. The inside of the robot chamber is painted red to reflect the light. We selected the red color because the photocells are least sensitive to the red wavelength (700 nm) to avoid chattering in the photocell's outputs when the robot vibrates during a motion. The outer surface of the robot is painted black to prevent infiltration from ambient light. We used a mixture of Smooth-On color Silc Pigment, Psycho Paint, and Novocs solvent which can be painted on silicone surfaces. The colors painted can be seen in Fig. 1. When the robot is operating, the reflection from the inner wall of the robot body will vary and the level of bending and turning will be reflected in the output voltages from each photocell. Fig. 3 shows the signals from each photocell as the robot is inflated from 6.89 kPa (1 PSI) to 20.68 kPa (3 PSI), then subsequently deflated back to 6.89 kPa, undergoing a free space motion.

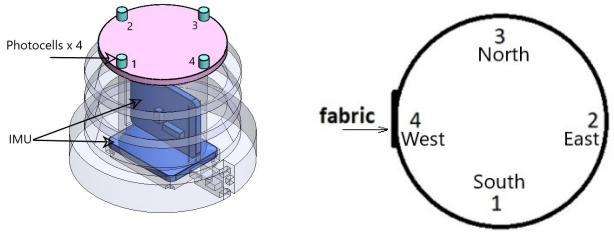

(a) (b)

Fig. 2. The sensing configuration: (a) The cap with the sensors; (b) The position of the photocells at the cap and direction labels for contact characterization (at all discs)

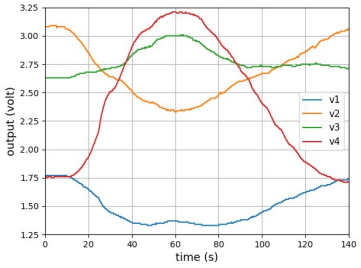

Fig. 3. Responses of the photocells during Squishy's operation: V_1, V_2, V_3, V_4 are the output voltages from photocell 1, photocell 2, photocell 3, and photocell 4, respectively

B. IMUs

A popular method to track the orientation of an object is using IMUs; they have low cost, low latency, and need no line-of-sight [21]. For our soft robot with a deformable body, the tip's orientation calculated using the light sensors is possible but there is the possibility for errors. However, the IMU gives us the signal directly, with reliable accuracy. We chose BNO005 which is a 9-DOF sensor that has an embedded fusion algorithm to provide orientation and other data from an accelerometer, magnetometer, and gyroscope. However, a key drawback of BNO005 (and any IMU) is drift.

We found that only the yaw data from the chosen IMU has large drifts, whereas the pitch and roll signals are stable. The reason is that the embedded sensor fusion can help compensate for drifts relating to pitch and roll well by measurements from the accelerometer sensing earth's gravity; whereas yaw drift is not well compensated by the measurement from the magnetometer sensing earth's magnetic field. To avoid the drift, we use a pair of BNO005s, installed perpendicular to one another inside the cap at the tip of the robot as shown in Fig. 2a. In this configuration, the drift-prone yaw signals are unused. The pitch of the second IMU is used in place of the yaw signal of the first. Hence, we can access the full orientation data of the robot tip without drifting. Because the state of the robot tip varies when the robot is contacted, the IMUs also contribute richer information in the training process for Squishy to learn the contact events.

C. The Pressure Sensor

We use a Honeywell pressure sensor (SSC-SANN001BGAA5) to measure the pressure inside the robot chamber. Its working range is from 0 to 100 kPa. The sensor provides feedback pressure information for the robot control and a feature for the contact training process.

III. Measuring the Pose of the Soft Robot

A. Squishy's Geometry

The robot is a circular chamber made of silicone. The longitudinal shape of the chamber is a quadrant of an annulus. It contains an embedded fabric on its left side which has the same radius R. The full dimensions of the robot in the undeformed state can be found in Fig. 4a. We installed the robot vertically, with disc 1 fixed to a bench and the tip closed by a cap. The initial state was set at 6.89 kPa. The initial curve's radius of the robot is R_0 which is smaller than the undeformed R, due to gravity. The operation of the robot during the inflation process includes two major motions: changing its curve's radius R from the initial radius R_0 and turning angle α (see Fig. 4b). Therefore, we can reconstruct the robot using the Piece-wise Constant Curvature (PCC) modeling approach [22] that characterizes a robot's pose based on its bending and turning motion.

To compare the measured pose of the robot with the ground truth and to address the contact localization spanning along the body of this soft robot, we discretized it into a series of discs (4 discs for this test case (see Fig. 4a)). The first and last discs are at the base and the tip of the robot, correspondingly. This discretization allows a more detailed illustration of the robot's shape so that more contact locations along the robot's body can be addressed, compared to the original PCC model. The robot is assumed to:

- Have all the disc centers lie along the same circular arc.
- Have no lateral bending (e.g. transverse to the fabric reinforcement).

The position of the center of each disc distal to disc 1 can be defined through the PCC parameters (R, ϕ_i, α), where ϕ_i is the bending angle between disc $i+1$ and disc 1 (see Fig. 4a).

For the bending motion, because the robot is equally divided into parts, each bending angle ϕ_i between disc $i+1$ $(i \in N, i \in [1,3])$ and disc 1 (the base) is calculated from $\phi_i = \frac{i\phi_3}{3}$ with $\phi_3 = \frac{L}{R}$.

The robot, when inflated, will deform so as to turn about the Z axis. The turning angle α is defined as the angle between the current plane containing the robot and the XZ plane in which the undeformed robot lies (see Fig. 4b).

Given the bending radius and turning angle of the robot, the location of each disc can be defined using the following usual homogeneous transformation from the arc base to the current disc [22]:

$$ {}^{1}T_{i+1} = \begin{bmatrix} R_z(\alpha) & 0 \\ 0 & 1 \end{bmatrix} \begin{bmatrix} R_y(\phi_i) & {}^{1}p_{i+1} \\ 0 & 1 \end{bmatrix} \tag{1} $$

where $R_z(\alpha)$ is the rotation matrix about Z axis in the world frame and $R_y(\phi_i)$ is the rotation matrix about y axis in the local frame. ${}^{1}p_{i+1}$ is the in-plane position of each disc center given as:

$$ {}^{1}p_{i+1} = \begin{bmatrix} R(1-\cos(\phi_i)) & 0 & R\sin(\phi_i) \end{bmatrix}^T \tag{2} $$

Proceeding with the multiplication, the homogeneous transformation has the following form:

$$ {}^{1}T_{i+1} = \begin{bmatrix} T_{i11} & T_{i12} & T_{i13} & T_{i14} \\ T_{i21} & T_{i22} & T_{i23} & T_{i24} \\ T_{i31} & T_{i32} & T_{i33} & T_{i34} \\ 0 & 0 & 0 & 1 \end{bmatrix} \tag{3} $$

where the individual elements are as follow:

$$ \begin{aligned} T_{i11} &= \cos(\alpha)\cos(\phi_i) & T_{i23} &= \sin(\alpha)\sin(\phi_i) \\ T_{i12} &= -\sin(\alpha) & T_{i24} &= R\sin(\alpha)(1-\cos(\phi_i)) \\ T_{i13} &= \cos(\alpha)\sin(\phi_i) & T_{i31} &= -\sin(\phi_i) \\ T_{i14} &= R\cos(\alpha)(1-\cos(\phi_i)) & T_{i32} &= 0 \\ T_{i21} &= \sin(\alpha)\cos(\phi_i) & T_{i33} &= \cos(\phi_i) \\ T_{i22} &= \cos(\alpha) & T_{i34} &= R\sin(\phi_i) \end{aligned} \tag{4} $$

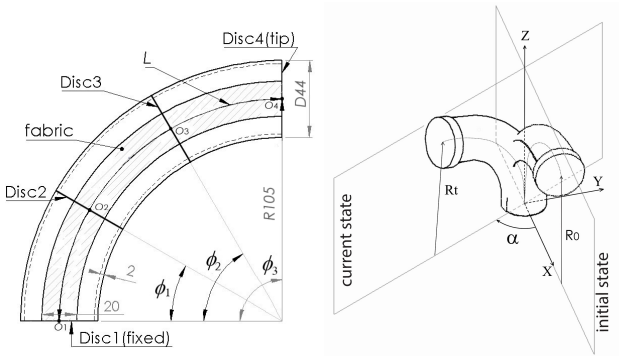

(a) 2D drawing with bending angles (ϕ_i) and dimensions of the soft robot

(b) 3D model of the robot at the initial state and current state with the turning angle (α) and curve's radius (R)

Fig. 4. Robot's dimensions and PCC parameters

B. Calculation of PCC Parameters

One important task in measuring the robot using this sensing approach is to define the correspondence between the bending and turning motions and the signals at each photocell. By observing the responses of the photocells in Fig. 3 and comparing them to the bending and turning calculated from the ground truth data, we got good agreements from the empirical fit after some trials to find a combination of the photocell signals that best represent the robot's motions. The fitting process shows that the two free-space motions of the robot can be represented by a combination of the outputs from photocells 3 and 4 according to the following equations:

$$ V_b = e^{(V_3+V_4)} \tag{5} $$

$$ V_t = e^{(V_3+V_4^{1.4})} \tag{6} $$

where V_b is the signal with the unit of voltage that represents bending and V_t is the one that represents turning motion.

Inspired by the work in [9], we developed analytical equations to calculate the two major PCC parameters: the

chamber's radius $R(t)$ and the turning angle $\alpha(t)$, using the voltages measured by the photocells. First, we use equation (7) to describe the relationship between the chamber's radius R and the bending voltage.

$$\left(\frac{V_b(t)}{V_{b0}}\right)^{\beta_b} = \ln\frac{R(t)}{R_0} + 1 \tag{7}$$

where V_{b0} is the voltage measured with the robot at the initial state in free space with a chamber pressure of 6.89 kPa, $R(t)$ the chamber's current radius, R_0 the initial radius. The tuning parameter β_b allows us to shift the bending signal in the calibration process.

Given the output voltage representing bending level $V_b(t)$, the current radius of the robot chamber can be calculated by inverting equation (7) as:

$$R(t) = R_0.e^{\left(\frac{V_b(t)}{V_{b0}}\right)^{\beta_b}-1} \tag{8}$$

In the same manner as with equation (7), the relationship between the turning angle $\alpha(t)$ and the turning voltage is given by equation (9)

$$\left(\frac{V_t(t)}{V_{t0}}\right)^{\beta_t} = \ln\frac{\alpha(t)}{\alpha_0} + 1 \tag{9}$$

where V_{t0} is the initial turning voltage, $\alpha(t)$ the current turning angle, α_0 the initial turning angle. β_t is the added tuning parameter allowing us to shift the turning signal in the calibration process. Finally, by inverting equation (9), the turning angle is calculated as:

$$\alpha(t) = \alpha_0.e^{\left(\frac{V_t(t)}{V_{t0}}\right)^{\beta_t}-1} \tag{10}$$

The above equations calculate the spine of the robot and are valid for motions less than 12°. For larger working ranges, we can develop other equations and apply them to our new Disc-Thread model [23], which needs more computational load. The diameter D of each disc will also vary with the chamber pressure. When inflating, the radii of the free discs in the middle are approximated using pressure-based empirical equations. For the robot used in our experiments, the diameter of symmetric disc 2 and disc 3 (measured in cm) can be approximated by:

$$D_{2,3} = 5 + 0.003P + 0.001P^2 \tag{11}$$

with P is the pressure inside the chamber, measured in kPa. The fitting has a coefficient of determination ($\mathbf{R}^2$) as high as 0.99.

IV. Contact Localization and Training

This section describes how we collected contact data to train the robot using machine learning. The goal is to help the soft robot localize contacts at various locations along its body and from different directions using the equipped sensors. We realized that when we made contact with the robot at different positions and directions, it will cause different movements at its tip as well as deform its body shape in distinctive manners. With the IMUs at the tip and the optical sensing working along the whole body, all changes in the robot's states during a contact event can be fully recognized. To build the data set for the training process, we pushed the robot at different locations and directions. Even though the contacts can be performed at any position along the body, in this test case, we discretized the robot into four discs and set a plan to make contact with the robot at the three distal-most discs (as disc 1 is stationary). At each disc, the contacts were made in four different directions, including the contact at "East", "West", "South", and "North" point (see Fig. 2b), with the contact force directed toward the center of the disc. Note that the "West" point is aligned with the fabric and the "South" point is facing the ground. A virtual bounding sphere is set around the free-space position of the tip corresponding to the current pressure. The radius of this sphere is selected after some contact experiments to examine the translation of the robot's tip. Whenever the center of the tip disc falls outside the bounding sphere, a contact event is detected. Based on that, we ran ten trials for each contact case and recorded the data from the sensors. The same process is repeated to generate data for different contact cases at different pressure values (6.89, 10.34, 13.78, 17.23, and 20.68 kPa), locations, and directions. In this experiment, four contact directions at three discs result in a total of twelve classification labels. The training features include the chamber's pressure, Euler angles from the IMUs, and four photocell voltages. The complete data set was then split into 80% for training and 20% for testing.

A set of classifiers were tested in this step including Logistic Regression, Naive Bayes, Support Vector Machine, K-Nearest Neighbors, Decision Tree, and Random Forest (RF). Random Forest Classification [24] resulted in the highest training score (96%) among all the classifiers tested. Hence, we selected RF classification for our work. In addition to the highest accuracy score for this data set, this algorithm is fast and effective for real-time training purposes [25]. The comparison between the performance of all the classifiers tested and the fusion matrix resulting from RF classification is shown in Fig. 5.

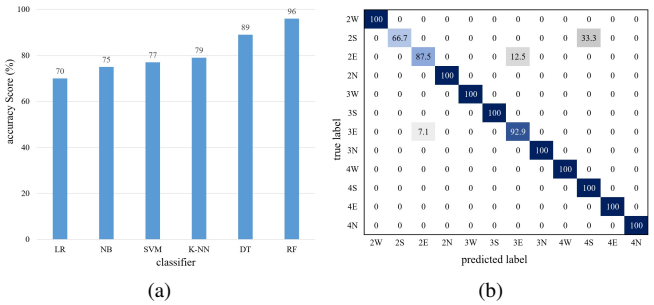

(a) (b)

Fig. 5. Training result: (a) Classifier comparison: LR = Logistic Regression, NB = Naive Bayes, SVM = Support Vector Machine, K-NN = K-Nearest Neighbors, DT = Decision Tree, and RF = Random Forest; (b) Fusion matrix: the numbers in the labels are for the disc number and the following letters are abbreviations for the directions. W = West, S = South, E = East, N = North

With the data collected directly from the embedded sensors, by recurring the RF classification, we can perform real-

time training for the robot to learn various contact cases. For that purpose, we developed a user interface by Python which allows us to contact the robot the way we want and save the contact data instantly. This work is important to help the robot perceive new types of contacts in new environments.

V. Results

As stated in Section III-B, the chamber radius R and the turning angle α can be calculated from the outputs of the photocells, specifically through equation (8) and equation (10). Having R and α, together with the chamber pressure P and the fabric lengths L, the discs representing the current shape of Squishy are defined by the homogeneous transformation in equation (3). In order to validate our calculation, we measured the ground-truth data using an electromagnetic motion tracking system (Polhemus Liberty) to compare with the results. To synchronize the ground-truth data and our calculation, we set the same start point and the same sampling rate at 5 Hz for all sensors. The soft robot was measured while it was moving in free space making a turning angle around 9° and turning back. This working range was set to assure that the soft robot will last for a longer working time. The first result of the calculation for major PCC parameters during a motion of the robot in the free space is depicted in Fig. 6. In this figure, the calculated chamber's radius and turning angle are well-fitted to those of the ground-truth data. It is noticed that there are some lags in the sensor responses at some points. This is because the wall of the robot is expandable, which sometimes balances the light changing caused by the bending and turning motion of the robot. However, the lags are small and will disappear when the robot is in a static state.

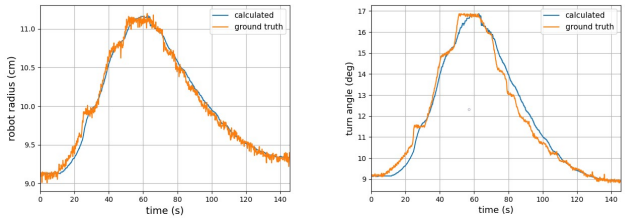

(a) Robot's radius (R) fitting (b) Turning angle (α) fitting

Fig. 6. Validation of PCC parameters

Fig. 7 illustrates the alignment between the calculated pose and the ground-truth pose at different pressure values. Note that the calculated pose is the animation with blue discs and centers and the ground-truth pose is the one with red discs and centers. We can see that all the disc centers at each disc location are close together. Note that the location of each disc and its center can be found in Fig. 4a.

The result from our measurement is also validated through the pose errors which are represented by the distances between the disc centers of the calculated pose and those of the ground-truth pose, as shown in Fig. 8. All the observed errors are less than 0.7 cm. There are several peaks but they are very brief. The calculated average errors for O_2, O_3, and O_4 are 0.174, 0.227, and 0.237 cm, correspondingly.

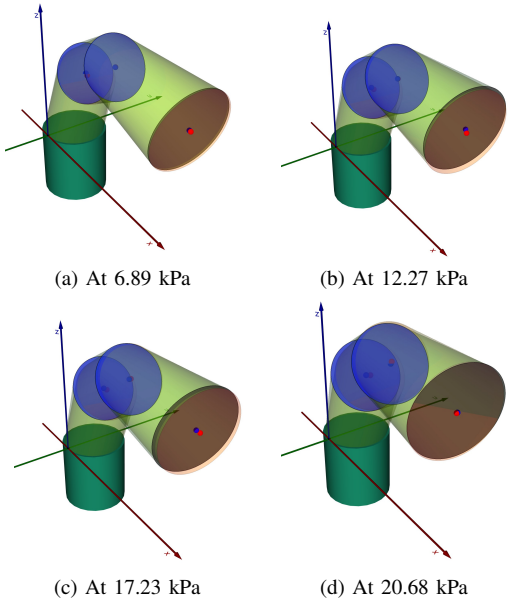

(a) At 6.89 kPa (b) At 12.27 kPa

(c) At 17.23 kPa (d) At 20.68 kPa

Fig. 7. Validation of the sensing approach at different pressure values. The calculated pose is the robot with blue discs and center points. The ground-truth is the robot with red discs and center points

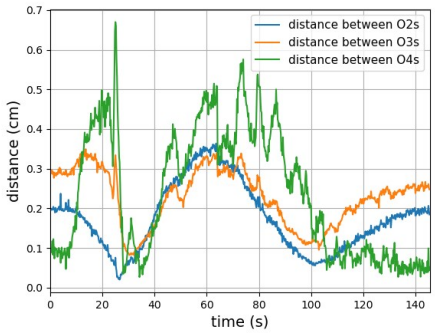

Fig. 8. The errors between the calculated pose and the ground truth

The result from the online training process for contact characterization is illustrated in Fig. 9. Of all the examples tested, we selected four representative cases to show here. Additional contact cases can be found in the attached video. In each sub-figure, the actual contact is shown in the photograph on the left, and the contact identified by the algorithm is illustrated by the red arrow in the frame from the animation shown on the right. Notice how the two seem to agree well where the contacts have been well-localized case by case. This measuring approach certainly allows us to perform contact localization at more places with higher computational load trade-offs. This achievement would support the robot control system in providing more suitable control actions adaptive to each specific contact case defined. Note that this work is only to define the contact position and direction. The pose of the robot during the

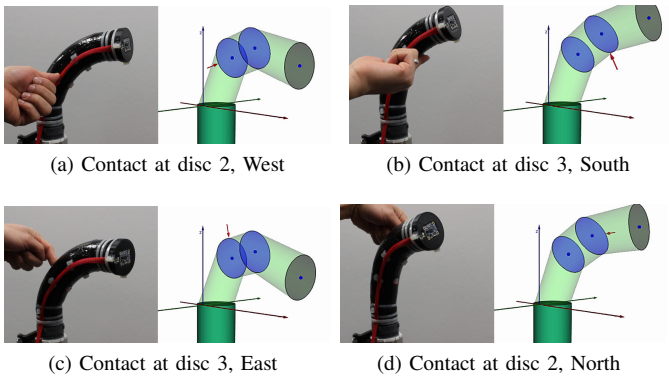

(a) Contact at disc 2, West (b) Contact at disc 3, South

(c) Contact at disc 3, East (d) Contact at disc 2, North

Fig. 9. Some contact localization at 12.78 kPa

contacts cannot be properly tracked by the optical sensors using PCC modeling anymore because the shape of the robot violates the PCC assumptions. Tracking the robot pose in contact cases is another challenging work and is not within the scope of this paper.

VI. Conclusion

The work in this paper provides a means for tracking the robot in free space and localization of contact events, using optical sensors, IMUs, and a pressure sensor. The sensing devices are affordable and widely available. We used a pair of orthogonal IMUs to avoid drift. The entire bore of the robot is used to transmit the light from the LED at the base to the photocells at the tip. This configuration utilizes the deformable characteristic of the soft robot to define contact events. Analytical equations are developed to characterize PCC parameters from the signals of optical devices. When compared against motion capture measurements, the results show that the sensor set has successfully tracked the pose of the robot in the free space with an average error of less than 0.3 cm. When the robot makes contact with the environment, the proposed sensors provide a rich data set that serves the training process well so that all the contact events are localized with a correctness of 96%. This sensing approach can be an alternative to tactile sensing skin for soft robots. The future works will be about the application of our new Disc-Thread model to track the pose of the soft robot during a contact event and the estimation of contact forces.

References

[1] D. Rus and M. T. Tolley, "Design, fabrication and control of soft robots," *Nature*, vol. 512, pp. 467–475, 2015.

[2] Z. Shen, H. Z. Y. Zhao, K. Tang, Y. Chen, Y. Xiao, J. Yi, S. Liu, and Z. Wang, "Soft Origami Optical-Sensing Actuator for Underwater Manipulation," *Front. Robot. AI*, vol. 7, p. 616128, 2021.

[3] S. Russo, T. Ranzani, H. Liu, S. Nefti-Meziani, K. Althoefer, and A. Menciassi, "Soft and stretchable sensor using biocompatible electrodes and liquid for medical applications," *Soft Rob.*, vol. 2 (4), p. 146–154, 2015.

[4] J. Morrow, H. S. Shin, C. P. Grafflin, S. H. Jang, J. Torrey, R. Larkins, S. Dang, Y. L. Park, and D. Berenson, "Improving soft pneumatic actuator fingers through integration of soft sensors, position and force control, and rigid fingernails," in *2016 IEEE international conference on robotics and automation (ICRA)*, Stockholm, Sweden, May 2016, p. 5024–5031.

[5] Z. Shen, J. Yi, X. Li, L. H. P. Mark, Y. Hu, and Z. Wang, "A soft stretchable bending sensor and data glove applications," *Rob. Biomimetics*, vol. 3 (1), p. 22, Apr 2016.

[6] R. A. Bilodeau, E. L. White, and R. K. Kramer, "Monolithic fabrication of sensors and actuators in a soft robotic gripper," in *2015 IEEE/RSJ international conference on intelligent robots and systems (IROS)*, Hamburg, Germany, Sep-Oct 2015, p. 2324–2329.

[7] N. Farrow, L. McIntire, and N. Correll, "Functionalized textiles for interactive soft robotics," in *2017 IEEE international conference on robotics and automation (ICRA)*, Singapore, May-June 2017, p. 5525–5531.

[8] M. C. Yuen, R. Kramer-Bottiglio, and J. Paik, "Strain sensor-embedded soft pneumatic actuators for extension and bending feedback," in *2018 IEEE international conference on soft robotics (RoboSoft)*, Livorno, Italy, April 2018, p. 202–207.

[9] C. To, T. L. Hellebrekers, and Y. Park, "Highly Stretchable Optical Sensors for Pressure, Strain, and Curvature Measurement," in *2015 IEEE/RSJ International Conference on Intelligent Robots and Systems*, Hamburg, Germany, Sep-Oct 2015, pp. 5898–5903.

[10] S. Sareh, Y. Noh, M. Li, T. Ranzani, H. Liu, and K. Althoefer, "Macrobend optical sensing for pose measurement in soft robot arms," *Smart Mater. Struct.*, vol. 24(12), p. 125024, 2015.

[11] H. Zhao, K. O'Brien, S. Li, S. Li, and R. F. Shepherd, "Optoelectronically innervated soft prosthetic hand via stretchable optical waveguides," *Sci. Rob.*, vol. 1(1), p. eaai7529, 2016.

[12] J. L. Molnar, C. A. Cheng, L. O. Tiziani, B. Boots, and F. L. Hammond, "Optical sensing and control methods for soft pneumatically actuated robotic manipulators," in *2018 IEEE international conference on robotics and automation (ICRA)*, Brisbane, QLD, May 2018, pp. 1–8.

[13] W. Chen, C. Xiong, C. Liu, P. Li, and Y. Chen, "Fabrication and dynamic modeling of bidirectional bending soft actuator integrated with optical waveguide curvature sensor," *Soft Rob.*, vol. 6(4), p. 495–506, 2019.

[14] W. Felt, K. Y. Chin, and C. D. Remy, "Smart Braid Feedback for the Closed-Loop Control of Soft Robotic Systems," *Soft Rob.*, vol. 4(3), pp. 261–273, Sep 2017.

[15] M. A. Mousa, M. Soliman, M. A. Saleh, and A. G. Radwan, "Tactile sensing biohybrid soft E-skin based on bioimpedance using aloe vera pulp tissues," *Sci. Rep.*, vol. 11, p. 3054, Sep 2021.

[16] B. Shih, D. Shah, J. Li, T. G. Thuruthel, Y. L. Park, F. Lida, Z. Bao, R. Kramer-Bottiglio, and M. T. Tolley, "Electronic skins and machine learning for intelligent soft robots," *Sci. Rob.*, vol. 5(41), Apr 2020.

[17] L. V. Duong and V. A. Ho, "Large-Scale Vision-Based Tactile Sensing for Robot Links: Design, Modeling, and Evaluation," *IEEE Transactions on Robotics*, vol. 37(2), pp. 390–403, Apr 2021.

[18] P. D. H. Bui and J. Schultz, "States and Contact Forces Estimation for a Fabric-Reinforced Inflatable Soft Robot," in *IEEE-RAS International Conference on Robotics and Automation*, Xi'an, China, October 2021, pp. 11 820–11 826.

[19] ——, "A Semilinear Parameter-Varying Observer Method for Fabric Reinforced Soft Robots," *Front. Robot. AI*, vol. 8, p. 749591, 2021.

[20] J. G. Williamson, C. Schell, M. Keller, and J. Schultz, "Extending the reach of single-chamber inflatable soft robots using Magnetorheological Fluids," in *IEEE International Conference on Soft Robotics*, New Haven, Connecticut, April 2021, pp. 119–125.

[21] F. Wittmann, O. Lambercy, and R. Gassert, "Magnetometer-Based Drift Correction During Rest in IMU Arm Motion Tracking," *Sensors*, vol. 19, p. 1312, March 2019.

[22] R. J. Webster and B. A. Jones, "Design and kinematic modeling of constant curvature continuum robots: A review," *Int. J. Rob. Res.*, vol. 29, p. 1661–1683, 2010.

[23] J. A. Schultz, H. Sanders, P. D. H. Bui, and M. Killpack, "Modeling the dynamics of soft robots by discs and threads," in *2022 IEEE international conference on robotics and automation (ICRA)*, Philadelphia, USA, May 2022, p. to appear.

[24] L. Breiman, "Random Forests," *Machine Learning*, vol. 45, pp. 5–32, 2020.

[25] F. Palermo, J. Konstantinova, K. Althoefer, S. Poslad, and I. Farkhatdinov, "Automatic Fracture Characterization Using Tactile and Proximity Optical Sensing," *Front. Robot. AI*, vol. 7, p. 513004, 2020.